Engineering Structures 318 (2024) 118786

Contents lists available at ScienceDirect

Engineering Structures

journal homepage: www.elsevier.com/locate/engstruct

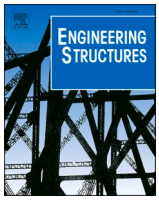

Lateral resistances of RC shear walls controlled by shear and sliding failure modes under axial tension

Ya-Bo Ding [a,b], Hui Chen [a,b,*], Jing-Ming Sun [a,b,*], Wei-Jian Yi [a,b], Zhongguo John Ma [c], Yun Zhou [a,b]

[a] College of Civil Engineering, Hunan University, Changsha, China
[b] Hunan Provincial Key Lab on Damage Diagnosis for Engineering Structures, Changsha, China
[c] Department of Civil and Environmental Engineering, The University of Tennessee Knoxville, TN, USA

ARTICLE INFO

Keywords:
RC shear wall
Tension-shear tests
Test database
Numerical analysis
Shear models
Sliding model

ABSTRACT

This study delved into the shear and sliding performances of RC shear walls subjected to combined axial tension and lateral shear, which may occur at the bottom of high-rise buildings under strong earthquakes. An extensive database comprising 41 RC shear walls tested under tension-shear was established, and the tests were categorized based on their failure modes. The study evaluated existing shear and sliding resistance models based on the collected database and introduced novel models for both shear and sliding resistances. The coefficients of variation for ratios of tested-to-predicted capacities of the proposed shear and sliding models are 0.18 and 0.24, respectively, significantly lower than those of the existing shear models and sliding models. A parametric analysis was conducted on the proposed models and the code models, and finite element results were used for verification. The results indicated that the proposed models not only effectively captured the influence of shear span-to-depth ratio, concrete strength, reinforcement ratios, and axial tensile force on the shear and sliding capacities of RC shear walls, but also well reflected the transition of shear and sliding failure modes. Furthermore, a numerical analysis was conducted to explore the impact of flange width on the shear capacity of shear walls. The numerical results confirmed that the proposed shear model effectively reflects the enhanced shear capacity due to the presence of flanges. However, predictions by ACI 318–19 and JGJ 3–2010 noticeably underestimated this effect.

1. Introduction

Reinforced concrete (RC) shear walls are extensively utilized in high-rise buildings as vital components for resisting seismic and wind loads. They primarily withstand axial (compression or tension) forces, horizontal shear, and moments. Typically, the wall piers are subjected to an internal force state of compression-shear-bending. However, with the increasing height of modern buildings, shear walls may experience tension-shear-bending under intense seismic loads [1,2]. As shown in Fig. 1(a), when the coupling ratio of coupled shear walls is relatively high, the axial tensile force induced by shear forces of coupling beams in one bottom wall pier may exceed the axial compression generated by gravity loads. As shown in Fig. 1(b), under bidirectional seismic loads, wall piers of a core wall structure may experience the tension-shear-bending state due to out-of-plane moments and in-plane shear.

A notable failure in RC shear walls under axial tension occurred during the 8.8-magnitude earthquake in Chile on February 27, 2010, leading to the collapse of the 15-story Torre Alto Rio building [3]. While the precise causes of the building's overall collapse and the extensive damage to the shear walls on the first floor remain inconclusive [4–6], an inference can be drawn from the concentrated locations of steel rupture and anchorage failure on one side of the building. This suggests that the shear walls on that side were in a state of tension-shear-bending at the time of failure. .

A large number of shear performance tests [7–18] on RC shear walls under compression have been conducted, and scholars [19–26] have also established shear test databases for RC shear walls. Previous compression-shear tests indicate that RC shear walls controlled by shear failure generally exhibit poor ductility and energy dissipation capabilities. After peak shear loads, there is a significant degradation in stiffness and strength. The shear performance is influenced by concrete strength, axial compression ratio, aspect ratio (or shear span-to-depth ratio),

* Corresponding authors at: College of Civil Engineering, Hunan University, Changsha, China.
E-mail addresses: chenhui@hnu.edu.cn (H. Chen), sunjingming@hnu.edu.cn (J.-M. Sun).

https://doi.org/10.1016/j.engstruct.2024.118786
Received 3 February 2024; Received in revised form 10 June 2024; Accepted 12 August 2024

Nomenclature

a	distance from the point of horizontal load action to the bottom surface of the wall
A_{sb}	total area of boundary longitudinal reinforcement on both sides
A_{sb1}	area of boundary longitudinal reinforcement on one side
$A_{sb,c}$	area of compressive boundary longitudinal rebars
A_g	gross area of the wall cross-section
$A_{s\ tr}$	strut cross-sectional area
A_{sw}	total area of the vertical distributed web reinforcement
$A_{sw,c}$, $A_{sw,t}$	areas of vertical web rebars under compression and tension, respectively
A_w	gross area of the shear wall web
b_e	strut equivalent thickness
b_f	flange width of non-rectangular shear walls
b_w	web thickness of walls
c	compressed zone height
d_w	effective height of wall cross-section
f_c	axial compressive strength of concrete
f_c'	cylinder compressive strength of concrete
f_t	axial tensile strength of concrete
f_y	yield stress of steel rebar
f_{yh}	yield strength of horizontal distributed reinforcement
f_{yb}	yield strength of boundary longitudinal reinforcement
f_{yw}	yield strength of vertical distributed web reinforcement
h_f	flange thickness of non-rectangular shear walls
l_w	wall length in the horizontal direction
N	axial force of walls
N_t	target axial tensile load
V_{dd}	dowel resistance of the vertical rebars
V_{fd}	friction resistance
V_{id}	shear resistance of inclined rebars
V_s, V_{sl}	predicted shear and sliding strength of shear walls, respectively
V_t	measured peak shear load
z	length of the internal lever arm
α_c	coefficient related to the axial force in ACI 318–19
β_s	strut effective coefficient
ε_{bc}, ε_{wc}	maximum and minimum strains in compressive boundary element, respectively
ε_{bt}, ε_{wt}	maximum and minimum strains in tensile boundary element, respectively
ε_{yb}	tensile yield strain of boundary longitudinal rebars
ξ	normalized neutral axis depth
η_c, η_s	axial tensile ratios of concrete and rebars, respectively
θ	angle between diagonal strut and boundary longitudinal reinforcement
μ	friction coefficient
ρ_b, ρ_{bs}	boundary longitudinal reinforcement and stirrup ratios, respectively
ρ_h , ρ_v	horizontal and vertical distributed reinforcement ratios, respectively
σ_s	reinforcement stress
$\sigma_{sb,c}$	average stress in the compressive boundary longitudinal reinforcement
σ_{sv}	average tensile stress of vertical reinforcement
$\sigma_{sw,c}$, $\sigma_{sw,t}$	average stresses in compressive and tensile vertical web reinforcement, respectively

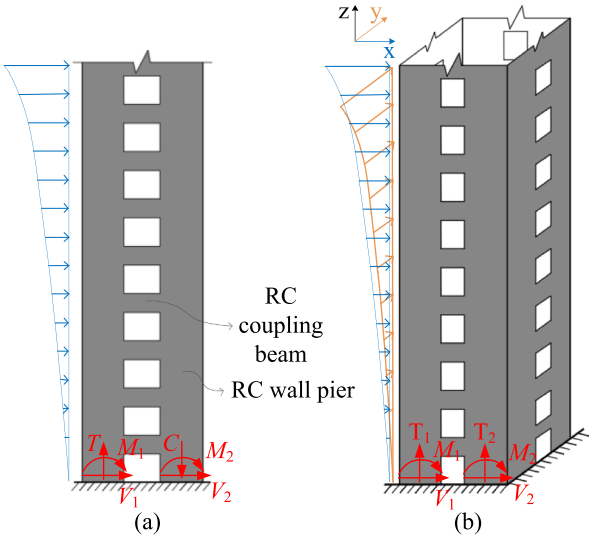

Fig. 1. Shear walls subjected to tension-shear-bending: (a) coupled shear wall under seismic loads; (b) wall core under bidirectional seismic loads.

boundary elements, and reinforcement ratio.

Research on RC shear walls under axial tension is relatively limited. In recent years, Wang et al. [27], Ren et al. [28], Xie [29], Ji et al. [1,30,31], Nie et al. [2], Yao et al. [32], and Wei et al. [33] conducted over forty tests on RC shear walls under the tension-shear state. Ke et al. [34] investigated the behavior of composite steel reinforced concrete (SRC) walls under tension-shear. The tension-shear test results indicate that an increase in axial tension significantly reduces the shear capacity, lateral stiffness, and energy dissipation capacity of shear walls. However, compared to shear walls failed in shear under axial compression, shear walls under the tension-shear state show an improvement in ultimate deformation capacity and exhibit better ductility. Nevertheless, existing experimental studies are limited to rectangular cross-section specimens, and there is a lack of research on the influence of flanges on the shear performance of RC shear walls under axial tension.

There is insufficient research on the failure mechanisms of shear walls under tension-shear conditions, and reliable shear and sliding capacity models are lacking. Existing shear and sliding models are mainly established for shear walls under shear-compression conditions. Although the shear and sliding strength models in structural design codes or standards can also be used for RC shear walls under tension-shear, their accuracy and safety have not been fully verified by sufficient experimental results.

Existing shear strength formulas for RC shear walls are mostly semi-empirical formulas based on the truss model. These formulas typically consider shear strength as the combined contribution of concrete and horizontal distributed reinforcement. The former is usually empirically fitted based on experimental data, while the latter is quantified based on the truss model. Design codes ACI 318–19 [35] and JGJ 3–2010 [36] generally do not provide separate shear strength equations for RC shear walls subjected to axial tension, but rather adjust the shear strength equations for shear walls under axial compression to account for the axial tension effect. Additionally, some scholars [2,37,38] have proposed modifications to existing code formulas specifically for shear walls subjected to axial tensile loads.

When RC shear walls are subjected to significant axial tensile loads coupled with cyclic lateral loads, it may lead to the formation of horizontal cracks that penetrate the entire cross-section, ultimately resulting in sliding failure. The sliding behavior of crack surfaces in reinforced

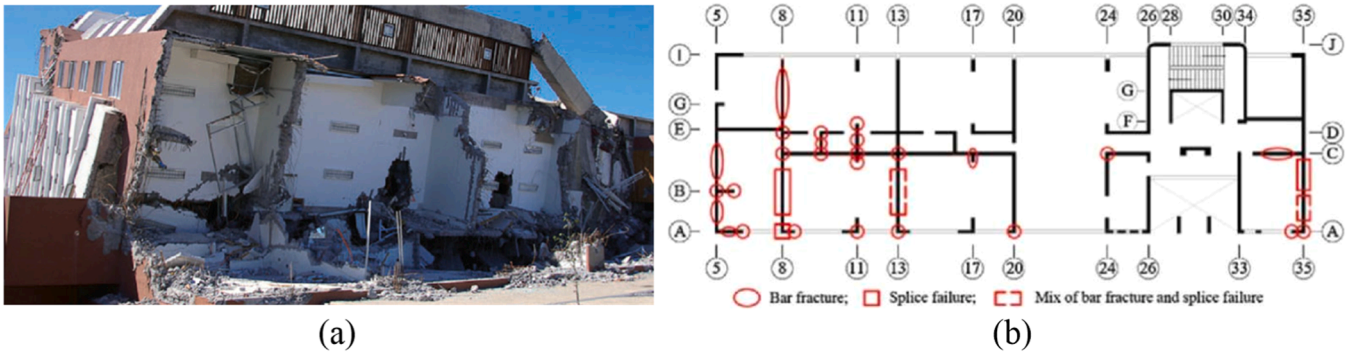

Fig. 2. Torre Alto Rio Building: (a) photograph after collapse [3]; (b) locations of steel rupture and splice failure on first floor [4].

Table 1
Test database of RC shear walls under tension-shear.

Shear wall Type	Authors and Reference	Specimen No.	$l_w \times b_w$ mm^2	a/d_w	ρ_b %	ρ_{bs} %	ρ_h %	ρ_v %	f_c' MPa	N_t kN	η_c	η_s	V_t kN	Failure Mode
1	Wang et al.	SW−1	1000 × 120	1.57	1.77	0.84	0.47	0.84	37.1	0	0.00	0.00	603	Shear
2	[27]	SW−2		1.57	1.77	0.84	0.47	0.84	37.1	176	0.39	0.08	543	Shear
3		SW−3		1.57	1.77	0.84	0.47	0.84	37.1	380	0.83	0.18	436	Shear
4		SW−4		1.57	1.77	0.84	0.47	0.84	37.1	578	1.27	0.27	427	Shear
5	Ren et al.	RCW17T100	800 × 120	1.61	0.69	0.79	0.39	0.59	66.2	157	0.34	0.22	231	Shear-Compression
6	[28]	RCW17T150		1.61	0.69	0.79	0.39	0.59	60.8	235	0.52	0.33	203	Shear-Compression
7		RCW17T200		1.61	0.69	0.79	0.39	0.59	66.5	303	0.65	0.43	184	Sliding
8		RCW17T250		1.61	0.69	0.79	0.39	0.59	58.9	390	0.88	0.55	174	Sliding
9		RCW17T350		1.61	0.69	0.79	0.39	0.59	58.5	548	1.23	0.77	130	Sliding
10		RCW25T000		1.61	1.14	0.79	0.39	0.59	50.1	0	0.00	0.00	404	Shear-Compression
11		RCW25T200		1.61	1.14	0.79	0.39	0.59	40.5	415	1.14	0.39	324	Shear-Compression
12		RCW25T250		1.61	1.14	0.79	0.39	0.59	48.5	579	1.39	0.55	260	Shear-Compression
13		RCW25T300		1.61	1.14	0.79	0.39	0.59	49.7	708	1.67	0.67	212	Sliding
14		RCW25T350		1.61	1.14	0.79	0.39	0.59	44.6	809	2.06	0.77	181	Sliding
15		RCW25T400		1.61	1.14	0.79	0.39	0.59	44.4	941	2.40	0.89	164	Sliding
16	Ji et al.	SW1	1500 × 180	1.22	1.25	0.56	0.37	0.58	49.7	617	0.52	0.25	960	Shear-Sliding
17	[1]	SW2		1.22	1.25	0.56	0.37	0.58	50.1	1030	0.86	0.41	823	Shear-Sliding
18		SW3		1.22	1.25	0.56	0.37	0.58	50.2	1716	1.42	0.69	568	Shear-Sliding
19		SW4		1.22	1.25	0.56	0.37	0.58	44.8	2553	2.30	0.76	337	Sliding
20		SW5		1.22	1.25	0.56	0.37	0.58	45.9	3192	2.83	0.95	282	Sliding
21		SW6		1.22	1.25	0.56	0.37	0.58	43.7	0	0.00	0.00	1173	Shear
22	Cheng et al.	SW7	1500 × 180	1.22	0.51	0.56	0.37	0.58	25.7	1148	1.69	0.76	153	Bending
23	[30]	HSW1		2.21	0.50	0.56	0.56	0.58	33.6	322	0.38	0.21	200	Flexural-Sliding
24		HSW2		2.21	0.50	0.56	0.56	0.58	22.0	538	0.89	0.35	189	Flexural-Sliding
25		HSW3		2.21	0.50	0.56	0.56	0.58	30.2	897	1.16	0.58	144	Flexural-Sliding
26		HSW4		2.21	0.50	0.56	0.56	0.58	25.7	1291	1.90	0.84	87	Bending
27	Ji et al.	MSW1	1500 × 180	1.67	0.84	0.56	0.37	0.58	24.5	582	0.86	0.20	749	Shear
28	[31]	MSW2		1.67	0.84	0.56	0.37	0.58	33.9	1163	1.34	0.39	552	Flexural-Shear
29		MSW3		1.67	0.84	0.56	0.37	0.58	36.4	1745	1.90	0.59	403	Bending
30		MSW4		1.67	0.84	0.56	0.37	0.58	25.7	2327	3.32	0.78	331	Bending
31	Nie et al.	T00	1700 × 150	1.14	1.19	1.34	0.38	0.38	49.1	0	0.00	0.00	1507	Shear-Compression
32	[2]	T30		1.14	1.19	1.34	0.38	0.38	49.1	776	0.70	0.28	1154	Shear-Compression
33		T40		1.14	1.19	1.34	0.38	0.38	49.1	1034	0.93	0.37	1105	Shear-Compression
34		T50		1.14	1.19	1.34	0.38	0.38	49.1	1293	1.16	0.46	1008	Shear-Compression
35	Yao et al.	W1	800 × 150	0.97	0.76	1.34	0.38	1.05	46.3	382	0.78	0.34	499	Shear
36	[32]	W2		0.97	1.03	1.34	0.38	2.05	46.3	696	1.34	0.41	605	Shear
37		W3		0.97	1.03	1.34	0.38	2.05	43.6	1044	2.10	0.62	517	Shear
38		W4		0.97	1.03	1.34	0.38	2.05	43.6	1392	2.80	0.83	468	Bending
39	Wei et al.	W4	1000 × 150	0.54	0.23	0.74	1.16	1.16	29.4	525	1.25	0.63	696	Shear
40	[33]	W11		0.54	0.23	0.74	0.74	1.16	29.4	525	1.25	0.63	520	Shear
41		W13		0.54	0.23	0.74	1.67	1.16	28.0	525	1.30	0.63	890	Shear

concrete structures is complex, and it is generally considered that the aggregate interlock and the dowel action of steel reinforcement together provide sliding resistances. Both the sliding strength formulas in ACI 318–19 and JGJ 3–2010 are based on the shear-friction theory, and their forms are also consistent, differing only in the values assigned to the friction coefficient and the axial force influence factor.

This paper established a tension-shear test database for RC shear walls and conducted a comprehensive and systematic analysis of their tension-shear performance. The tests were categorized based on reported failure modes, and their typical load-transfer mechanisms were demonstrated using refined finite element (FE) models. Existing shear and sliding resistance models were evaluated based on the database, and new shear and sliding models were proposed. Additionally, the impact of shear wall flanges on shear capacity was analyzed using FE models, and the predictions by the proposed shear model were validated.

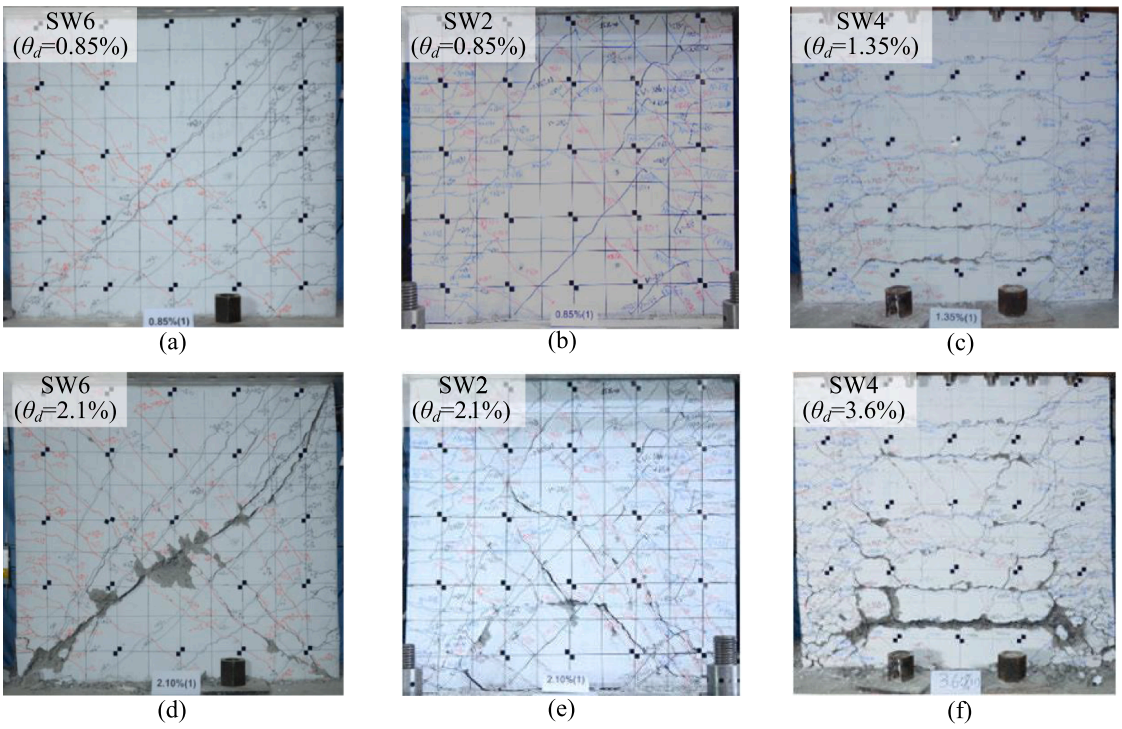

Fig. 3. Photographs of shear walls tested by Ji et al. [1]: (a) SW6, (b) SW2, and (c) SW4 at peak shear loads; (d) SW6, (e) SW2, and (f) SW4 after failure.

2. Failure mode and load-transfer mechanism

2.1. Test database

This study compiled 41 existing tension-shear tests of RC shear walls [1,2,27,28–33] (Table 1), all featuring rectangular cross-sections with shear span ratios not exceeding 2.21. The reported primary failure modes include flexural failure, shear failure (including shear and shear-compression), and sliding failure.

When the shear span ratio is relatively large, or the longitudinal reinforcement in the boundary elements is limited, shear walls are prone to flexural failure. Flexural-controlled shear walls exhibit predominant flexural deformations, demonstrating good ductility with plump hysteresis loops. Shear failure is more likely to occur in specimens with smaller shear span-to-depth ratios or higher longitudinal reinforcement ratios. The ductility of such shear wall specimens is relatively poorer compared to flexural-controlled ones but better than specimens experiencing shear failure in compression-shear tests. During shear failure, significant horizontal displacement occurs along critical shear cracks, with nearly all the horizontal distributed reinforcement intersecting with the critical cracks yielding. Sliding failure tends to occur in shear walls with higher axial tensile stresses, manifesting as significant lateral movement along a horizontal crack. While these specimens exhibit good ductility, their lateral load-carrying capacity is relatively low, and the hysteresis loops show significant pinching, indicating poor energy dissipation capability.

Additionally, the database includes a small number of shear wall specimens that have been reported to exhibit combined failure modes known as flexural-shear, flexural-sliding, and shear-sliding. For shear walls controlled by flexural-shear or flexural-sliding, after the boundary longitudinal rebars yield completely in tension, their flexural capacity tends to stabilize. With further increased deformation of the specimens, the shear or sliding capacity degrades faster than the flexural capacity. When the shear or sliding capacity falls below the flexural capacity, the shear walls transition from the flexural mechanism to the shear or sliding mechanism, ultimately resulting in the shear or sliding failure. The peak lateral resistances of shear walls with flexural-shear and flexural-sliding failures are still determined by the flexural capacity. Thus this study classifies them under flexural failure.

On the other hand, for shear walls controlled by shear-sliding failure, significant diagonal cracks can be observed at the peak load, and the specimen deformation is dominated by shear deformation. After reaching the peak horizontal load, a horizontal sliding surface forms under cyclic loading. The peak lateral resistance of specimens with shear-sliding failure is determined by the ultimate shear capacity, so the shear-sliding failure is categorized as shear failure in this study. Further clarification on this failure mode will be provided in Section 2.2 through a combination of experimental and FE results.

The database in Table 1 provides the cross-sectional dimensions (wall length l_w× wall thickness b_w), the ratio of shear span length to effective depth a/d_w (from 0.54 to 2.21), the boundary longitudinal reinforcement ratio ρ_b (from 0.23 % to 1.77 %), the boundary stirrup ratio ρ_{bs} (from 0.56 % to 1.34 %), the horizontal distributed reinforcement ratio ρ_h (from 0.37 % to 1.67 %), the vertical distributed web reinforcement ratio ρ_v (from 0.38 % to 2.05 %), and the measured cylinder concrete compressive strength f_c' (from 22.0 to 66.5 MPa) for each specimen. Additionally, N_t represents the target axial tensile force, which is the maximum value of axial force during the loading process; V_t is the measured peak shear load. The axial tensile ratio of concrete, η_c, of a cross-section under N_t equals $N_t/((A_c+(E_s/E_c)\bullet(A_{sb}+A_{sw}))\bullet f_t)$, and the axial tension ratio of rebars η_s equals to $N_t/(f_{yb}A_{sb}+f_{yw}A_{sw})$. Where A_c is the area of concrete at the cross-section, E_s and E_c are steel and concrete elastic moduli, respectively; A_{sb} and f_{yb} are the total area and yield strength of boundary vertical reinforcement, respectively; A_{sw} and f_{yw} are the total area and yield strength of vertical distributed web reinforcement, respectively; f_t is the axial tensile strength of concrete. In the database, the range of the concrete tensile ratio η_c is 0 to 3.32, and for η_s, it is 0 to 0.95.

2.2. Finite element modeling

To clarify the variations in the load-transfer mechanisms of shear walls with different failure modes under tension-shear, the commercial FE software ATENA was employed to simulate and analyze three shear

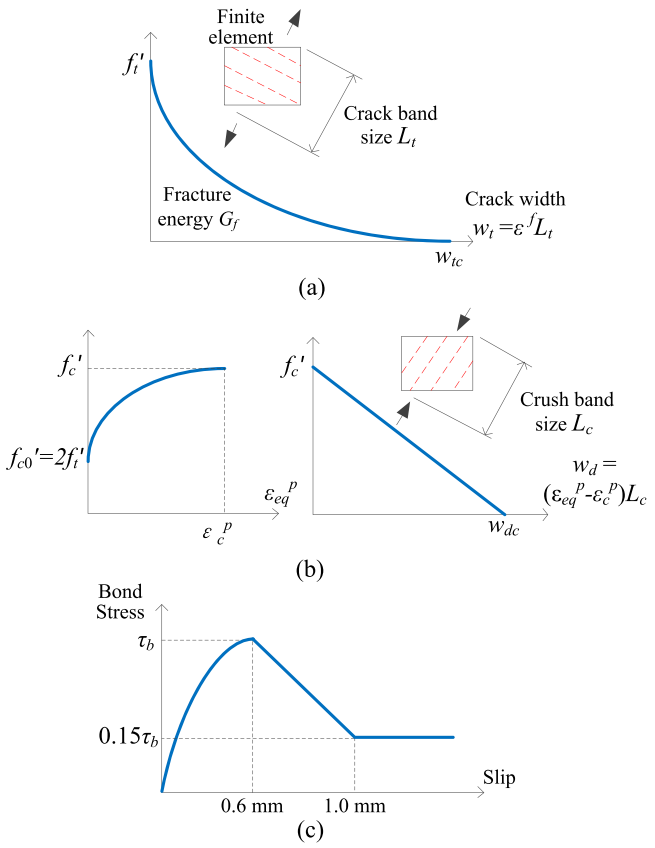

Fig. 4. Non-linearities in material constitutive relationships applied in numerical simulation. (a) Tensile softening for concrete after cracking, (b) Compressive hardening/softening for concrete, and (c) bond-slip relationship between concrete and steel reinforcement.

wall specimens (SW6, SW2, and SW4) tested by Ji et al. [1]. The target axial tensile loads N_t for the selected specimens SW6, SW2, and SW4 were 0, 1030, and 2553 kN, respectively, with reported failure modes of shear, shear-sliding, and sliding. For ease of comparison with numerical results, Fig. 3 provides photographs of these specimens at peak shear loads and after failure. In the figure, θ_d represents the lateral drift ratio, which is equal to the lateral displacement at the loading point divided by the vertical distance from the loading point to the top surface of the ground beam.

In the numerical simulation of the shear wall specimens, concrete was modeled using the fracture-plastic model [39], which combined constitutive models for tensile (fracturing) and compressive (plastic) behavior. The nonlinearities in the fracture-plastic concrete model, including tensile softening after cracking and compressive hardening/softening, are shown in Fig. 4(a) and (b) respectively. To better simulate the post-cracking behavior of concrete, the Rankine failure criterion with exponential crack opening law of Hordijk, and the Fixed Smeared Crack Model were employed. The crack width was determined based on the Crack Band method proposed by Bažant and Oh [40], which also effectively controlled the sensitivity of meshing size [41]. In compression, the Menetrey-Willam failure surface [42] is used for the hardening/softening plasticity model. Steel reinforcement was modeled by the bilinear hardening model. A bond-slip model between concrete and steel reinforcement [43] based on the CEB-FIP model code (1990) was also employed, as shown in Fig. 4(c). The influences of cracks on concrete compressive strength and crack interface shear strength were determined using the Modified Compression Field Theory (MCFT) [44,45]. The detailed descriptions of these constitutive models can be found in reference [46], and they were implemented in ATENA for the simulation of the selected specimens. ATENA has been extensively validated for reasonably simulating the shear behavior of concrete structures [41,47–50].

Fig. 5 shows the finite element model of the specimens SW6, SW2, and SW4. A 1/2 model was established using the symmetry of the specimens, and the out of plane displacement of the symmetry plane was constrained (Fig. 5(c)). Concrete was modeled using hexahedral solid elements, and the rebar was modeled using truss elements with a separate modeling method. Loading plates were modeled with quadrilateral solid elements and were tied to the surface of the loading beam. The bottom of the foundation beam was fixedly constrained, and horizontal displacement was applied at half the height of the rigid loading plate. Vertical uniformly distributed stress was applied to the bottom of the loading beam to simulate the axial tensile force. The concrete element size for the wall was approximately 50 mm × 50 mm × 45 mm, while the concrete element size for the loading and foundation beams was 100 mm × 100 mm × 100 mm. In solving the nonlinear equations, the Newton-Raphson method was used, combined with a line search method to improve convergence efficiency. The convergence criteria allowed a convergence error of 1 %, and the maximum number of iterations per step was set to 30. In order to further improve computational

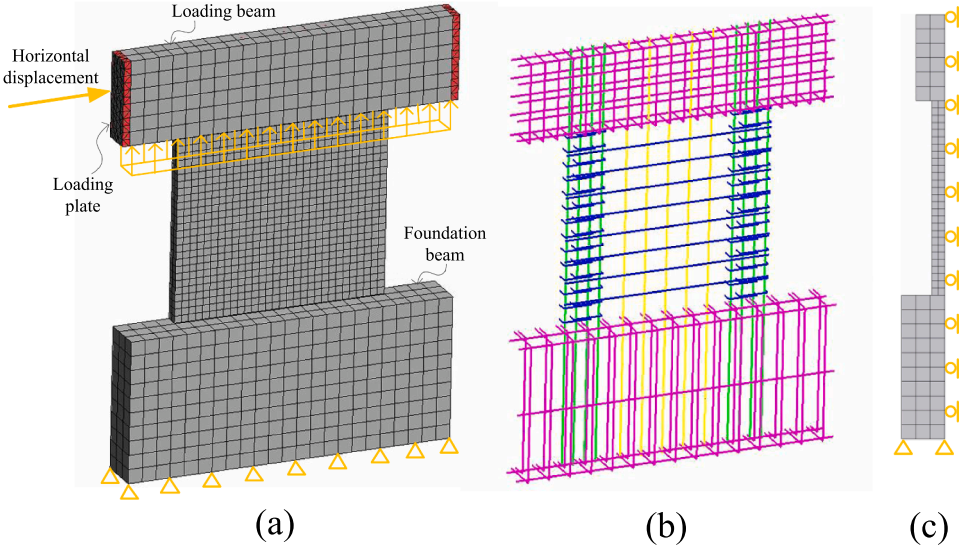

Fig. 5. Finite element model of specimens SW6, SW2, and SW4: (a) concrete elements and boundary conditions, (b) rebar elements, and (c) out-of-plane constraint.

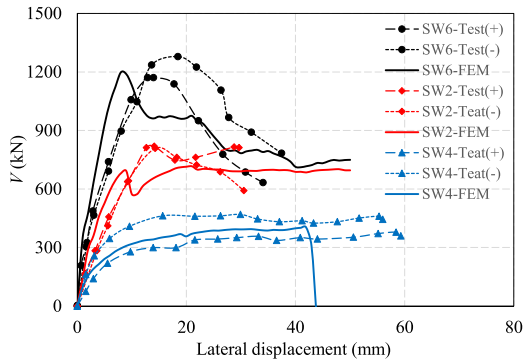

Fig. 6. Shear load-lateral displacement curves of selected shear walls.

efficiency, the finite element model was subjected to horizontal monotonic loading, with each step of horizontal loading controlled by a preset displacement.

Fig. 6 illustrates the skeleton curves of shear load-horizontal displacement for the selected shear walls (where "+" and "-" denote the positive and negative directions in cyclic tests, respectively) and the shear load-horizontal displacement curves obtained from FE models under monotonic loading. It can be observed that there is a good agreement between the two. The average values of the tested peak shear loads of the specimens SW6, SW2, and SW4 in the two directions are 1225 kN, 814 kN, and 424 kN, respectively, while the corresponding numerical results are 1198 kN, 716 kN, and 404 kN. The prediction errors are −2.21 %, −11.97 %, and −4.92 %, indicating that the FE models can well simulate the load-carrying and overall deformation capacities of shear walls under different target axial tensile loads.

Fig. 7(a-c) illustrates the crack distribution of the FE models for the selected specimens after failure. For the specimen SW6 with zero axial tension, significant diagonal cracks developed, and horizontal cracks at the bottom of the wall were effectively controlled, as shown in Fig. 7(a). The horizontal deformation of SW6 was concentrated mainly at the diagonal cracks, indicating a typical shear failure. For the specimen SW2 with the target axial load of 1030 kN, both diagonal cracks and bottom horizontal cracks were prominent (Fig. 7(b)), and the horizontal deformation of SW2 was dominated by shear deformation at the inclined cracks and sliding deformation at the bottom horizontal cracks. These observations are consistent with the reported shear-sliding failure mode for WS2. Specimen SW4, with the maximum target axial load, experienced sliding failure during the test. The FE model also exhibited predominant bottom horizontal cracks, while diagonal cracks were somewhat suppressed, as shown in Fig. 7(c). Horizontal deformation of the specimen was concentrated at the bottom sliding cracks. By comparing Fig. 7(a)-(c) and Fig. 3(d)-(f), it validates that the applied FE models can effectively simulate the observed crack patterns and failure modes of the selected shear walls subjected to different axial tensile loads in the test.

Based on the validated FE models, the principal stress distribution for the specimens SW6, SW2, and SW4 at peak loads are presented in Fig. 7 (d)-(f). It can be observed that when the target axial force is zero, the main shear load-transfer path for specimen SW6 is a significant diagonal

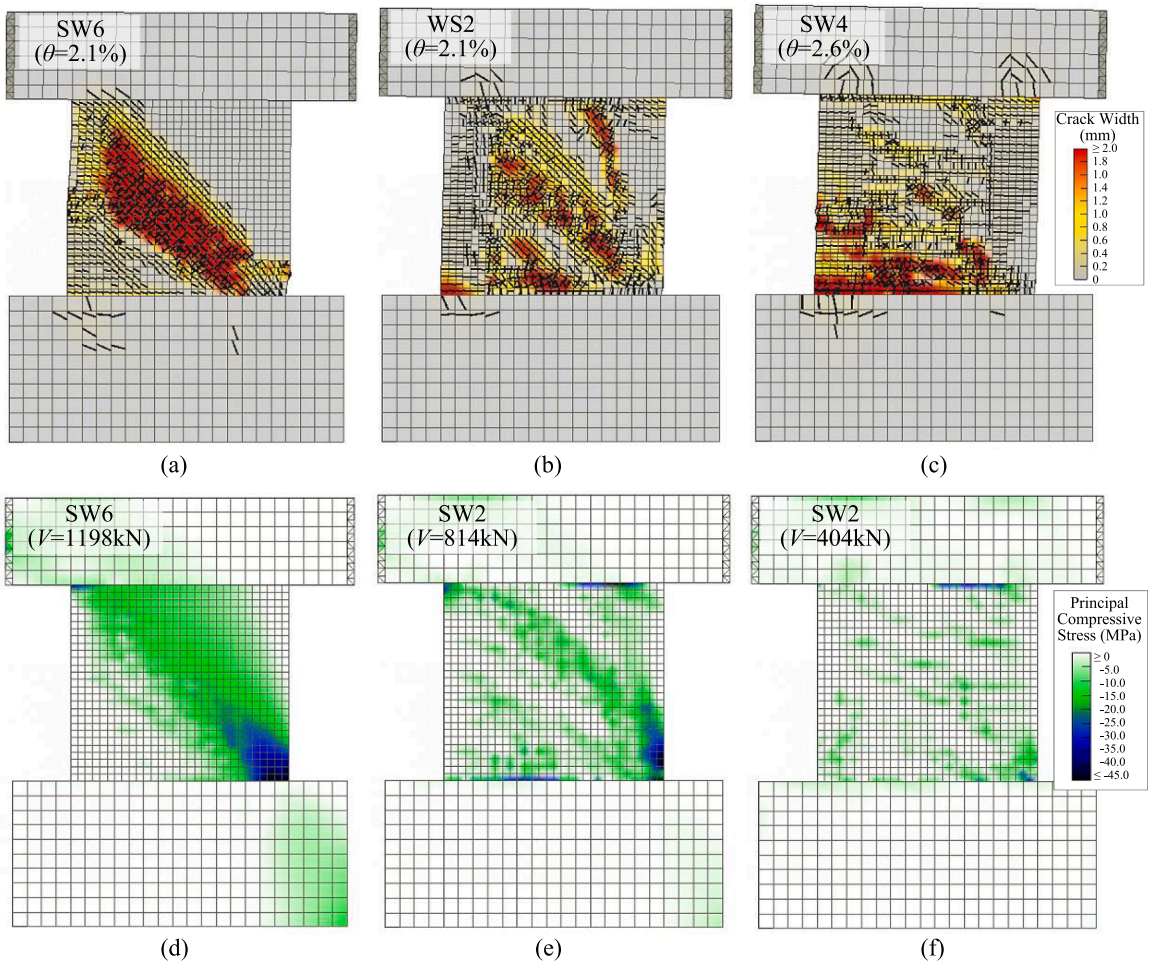

Fig. 7. Numerical results of selected shear walls: crack distribution of (a) SW6, (b) SW2, and (c) SW4 after failure; principal compressive stress distribution of (d) SW6, (e) SW2, and (f) SW4 at peak shear loads.

strut. This diagonal strut has a relatively large width, and the principal compressive stress values are relatively high, with the maximum principal compressive stress occurring at the bottom compression zone of the wall. As the target axial tensile load increases, as shown for specimens SW2 and SW4 in Fig. 7(e) and (f), the diagonal strut is gradually weakened, manifested by the decreasing width and stress values of the diagonal strut. For specimen SW4 with the maximum target axial tensile load, which failed in sliding, the diagonal strut is almost nonexistent within the wall at the peak shear load. Therefore, it can be assumed that the primary shear-transfer path for shear walls controlled by shear failure is the diagonal strut, which weakens with the increasing axial tension on the wall. On this basis, a mechanical model that considers the influence of axial tensile loads on the shear capacity of RC shear walls will be proposed in the next section.

3. Shear and sliding strength prediction models

3.1. Existing shear models

The shear strength, $V_{s,\ \mathrm{ACI}}$, of RC shear wall in the American code ACI 318–19 [35] (hereinafter referred to as ACI) is composed of the shear carried by concrete and horizontal distributed reinforcement, taking into account the influence of axial tension on the concrete resistance.

$$V_{s,ACI} = \left(\alpha_c \sqrt{f_c'} + f_{yh}\rho_h\right)A_w \le 0.66\sqrt{f_c'}A_w \tag{1}$$

$$\alpha_c = 0.17\left(1 - 0.29\frac{N}{A_g}\right) \ge 0 \tag{2}$$

where α_c is a coefficient related to the axial force, and when the axial force is in tension (positive value), its value is determined according to Eq. (2); A_w represents the gross area of the shear wall web; f_{yh} and ρ_h represent the yield strength and ratio of horizontal distributed reinforcement; f_c' is the cylinder concrete compressive strength, and A_g is the gross area of the wall cross-section. It should be noted that in this paper, the axial force N is consistently considered positive for tension and negative for compression.

In the Chinese code JGJ 3–2010 [36] (hereinafter referred to as JGJ), the formula for the shear resistance V_{JGJ} of RC shear walls is as follows:

$$V_{s,JGJ} = \frac{1}{a/d_w - 0.5}\left(0.4 f_t b_w d_w - 0.1N\frac{A_w}{A_g}\right) + 0.8\mathrm{f_{yh}}\rho_{\mathrm{h}} b_w d_w \tag{3}$$

where a/d_w is the shear span-to-depth ratio, with upper and lower limits taken as 1.5 and 2.2, respectively; f_t is the axial tensile strength of concrete; b_w is the web thickness of walls; d_w is the effective height of the wall cross-section.

Based on the JGJ shear model, Xiao et al. [37] introduced the influence of boundary longitudinal reinforcement and proposed the following equation for the shear strength $V_{s,\ \mathrm{Xiao}}$:

$$V_{s,Xiao} = \frac{1}{a/d_w - 0.5}\left(0.4 f_t b_w \mathrm{d_w} - 0.2N\frac{A_w}{A_g}\right) + 0.8\mathrm{f_{yh}}\rho_{\mathrm{h}} b_w d_w + 0.04 A_{sb1} f_{yb} \tag{4}$$

where A_{sb1} is the area of boundary longitudinal reinforcement on one side (when the areas of boundary longitudinal reinforcement on both sides are different, the smaller one is used), and f_{yb} is the yield strength of the boundary longitudinal reinforcement.

Cheng [38] made modifications to the axial force term in the JGJ shear equation and incorporated the contribution of vertical reinforcement (including boundary longitudinal reinforcement and vertical distributed web reinforcement) to the shear strength, $V_{s,\ \mathrm{Cheng}}$, of RC shear walls.

$$V_{s,\mathrm{Cheng}} = \frac{1}{a/d_w - 0.5}\left(0.4 f_t b_w d_w - 0.25N\frac{A_w}{A_g}\right) + 0.8\mathrm{f_{yh}}\rho_{\mathrm{h}} b_w d_w + \frac{0.15}{a/d_w}\left(A_{sb} f_{yb} + A_{sw} f_{yw}\right) \tag{5}$$

where the lower limit for the shear span-to-depth ratio a/d_w is 1.5; A_{sb} represents the total area of boundary longitudinal reinforcement on both sides; A_{sw} and f_{yw} are the total area and yield strength of the vertical distributed web reinforcement, respectively.

Eq. (6) proposed by Nie et al. [2] takes into account the dowel action of vertical reinforcement on the shear strength $V_{s,\ \mathrm{Nie}}$, and the adopted axial force influence factor is related to material strength and reinforcement ratio.

$$\begin{aligned} V_{s,\mathrm{Nie}} = {} & \max\left(\frac{0.508}{a/d_w} - 0.266, 0\right)\left(A_{sb} f_{yb} + A_{sw} f_{yw}\right) + \max\left(0.473 - 0.1a/d_w, 0\right) f_t b_w d_w \\ & + 0.7\mathrm{f_{yh}}\rho_{\mathrm{h}} b_w d_w - \left(0.113 + 0.501\frac{f_t b_w d_w}{A_{sb} f_{yb} + A_{sw} f_{yw}}\right)\mathrm{N} \end{aligned} \tag{6}$$

3.2. Proposed shear model

According to the numerical analysis in Section 2.2, the diagonal strut is the main shear-transfer path for shear walls controlled by shear failure. Yi et al. [51] proposed equations for the shear strength of squat shear walls under the compression-shear condition, which was derived based on the cracking strut-and-tie model [52,53]. The influences of stirrups, concrete strength, and size effect on shear strength were considered through the effective strut coefficient β_s. The effects of axial force and boundary longitudinal reinforcement were considered through the strut width (determined based on the compression zone height at the wall bottom cross-section). Additionally, the equations took into account the influence of the shape of the boundary members through the equivalent strut thickness (in the out-of-plane direction of the wall).

For RC shear walls controlled by shear failure, the main load-transfer paths under both tension-shear and compression-shear states are diagonal struts, but the width and effective compressive strength of the struts differ. Therefore, it is possible to derive the shear strength equations of shear walls under tension-shear based on the cracking strut-tie model.

Building upon the equations proposed by Yi et al. [51], the influence of axial tensile force on the compression zone height c is quantified to account for its impact on the shear strength. Additionally, for specimens with a high vertical web reinforcement ratio or a low boundary longitudinal reinforcement ratio, the original equations underestimate the actual shear strength of these shear wall specimens by neglecting the effect of vertical web reinforcement. Therefore, by considering the influence of vertical web reinforcement on c, this paper proposes the following modified equations for the shear strength $V_{s,p}$.

$$V_{s,p} = \beta_s f_c' A_{str} \sin\theta = \beta_s f_c' c b_e \sin\theta \tag{7}$$

$$\beta_s = 0.5(1+100\rho_h)^{0.8}\left(\frac{500}{d_w}\right)^{0.2}\left(\frac{30}{f_c'}\right)^{0.5} \le 0.85\left(1-\frac{f_c'}{250}\right) \tag{8}$$

$$\left(\frac{c}{d_w}\right)^2 + \left[1.5\frac{h_f}{d_w}\left(\frac{b_f}{b_w}-1\right)+1.5\frac{N}{b_w d_w f_c'}+600\frac{\rho_b+\rho_v}{f_c'}\right]\frac{c}{d_w} - 600\frac{\rho_b+0.5\rho_v}{f_c'} = 0 \tag{9}$$

$$b_e = b_w\left[1+0.5\frac{h_f}{c}\left(\frac{b_f}{b_w}-1\right)\right] \tag{10}$$

where β_s is the strut efficiency coefficient; A_{str} is the cross-sectional area of the strut; b_e represents the equivalent thickness of the strut; c represents the compression zone height at the bottom cross-section of the wall and is used to characterize the width of the strut at the bottom of the wall; θ is the angle between the diagonal strut and boundary longitudinal reinforcement, and can be taken as $\arctan((l_w\text{-}c/2)/a)$, where l_w is the length of the wall in the horizontal direction, and a is the distance from the application point of the lateral shear load to the bottom surface of the wall; h_f and b_f represent the thickness and width of the flange, respectively; ρ_b represents the ratio of boundary longitudinal reinforcement on one side, which is equal to $A_{sb1}/(b_w d_w)$; ρ_v is the vertical distributed web reinforcement ratio.

3.3. Existing sliding models

JGJ specifies that the sliding strength $V_{sl,JGJ}$ of the horizontal construction joints for shear walls with a seismic performance level of Level I should comply with the requirements of Eq. (11).

$$V_{sl,JGJ} = 0.6\left(A_{sb}f_{yb}+A_{sw}f_{yw}\right)-0.8N \tag{11}$$

ACI specifies that when the reinforcement is perpendicular to the shear plane, the sliding strength $V_{sl,ACI}$ of the shear plane is calculated according to the following equation:

$$V_{sl,ACI} = \mu\left(A_{sb}f_{yb}+A_{sw}f_{yw}-N\right) \le \min\left[0.2f_c'A_g,\ (3.3+0.08f_c')A_g,\ 11A_g\right] \tag{12}$$

where μ is the friction coefficient. According to ACI, for concrete placed monolithically, the friction coefficient μ is recommended to be taken as 1.4. However, this value appears to be too large for the sliding surface of shear walls subjected to combined axial tension and cyclic lateral loads. Therefore, following the concrete-to-concrete friction coefficient under cyclic actions in Eurocode 8 [54], μ is taken as 0.7.

The sliding strength $V_{sl,EC8}$ of a potential sliding plane in Eurocode 8 [54] is composed of friction resistance V_{fd}, shear resistance of inclined rebars V_{id}, and dowel resistance of the vertical rebars V_{dd}.

$$V_{sl,EC8} = V_{dd}+V_{id}+V_{fd} \tag{13}$$

$$V_{dd} = \min\left[1.3\left(A_{sb}\sqrt{f_c f_{yb}}+A_{sw}\sqrt{f_c f_{yw}}\right),\ 0.25\left(A_{sb}f_{yb}+A_{sw}f_{yw}\right)\right] \tag{14}$$

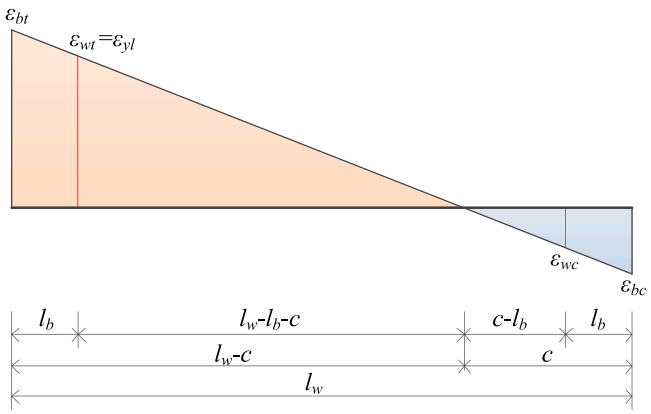

Fig. 8. Vertical strain assumption of sliding plane in proposed sliding model.

$$V_{fd} = \min\left(\mu\left[\left(A_{sb}f_{yb}+A_{sw}f_{yw}-N\right)\xi+\frac{M_{Ed}}{z}\right],\ 0.5\eta f_c\xi A_w\right) \tag{15}$$

where f_c is the concrete axial compressive strength; the friction coefficient μ is 0.7 for rough surfaces of concrete-to-concrete under cyclic actions; ξ is the normalized neutral axis depth and equals to c/l_w, where c can be determined according to Eq. (9); η is a coefficient equal to 0.6 $(1-fc/250)$; M_{Ed} is the design bending moment from the analysis for the seismic design situation, which is assumed to be zero in this study; and z is the length of the internal lever arm. The expression for V_{id} is not provided because the specimens in the collected database were not reinforced with inclined rebars.

Taking into account the possibility of asynchronous yielding of boundary longitudinal rebars and vertical web rebars, Xiao et al. [37] made modifications to the JGJ sliding model and proposed the following equations.

$$V_{sl,Xiao} = \max\begin{pmatrix} 0.6A_{sw}\left(f_{yw}-\sigma_{sv}\right) \\ 0.6A_{sb}\left(f_{yb}-\sigma_{sv}\right) \\ 0.6\left(A_{sb}+A_{sw}\right)\left[\min\left(f_{yb},f_{yw}\right)-\sigma_{sv}\right] \end{pmatrix} \tag{16}$$

where σ_{sv} represents the average tensile stress of the vertical reinforcement, which is equal to $N/(A_{sb}+A_{sw})$.

3.4. Proposed sliding model

For sliding failure-controlled RC shear walls, both the friction resistance of the concrete and the dowel action of vertical rebars on the sliding surface contribute to the sliding strength. From the perspective of shear-transfer mechanisms, the physical basis of the sliding model in Eurocode 8 is more robust. However, this model does not consider the weakening effect of axial stress generated by internal forces of shear walls on the dowel resistance of vertical rebars. Therefore, it overestimates the sliding strength of RC shear walls under tension-shear states, which is verified in Section 4.2.

Chen et al. [52,53] proposed a simplified reduction factor $(1\text{-}\sigma_s/f_y)$ to consider the interaction between the tensile force and the dowel force of steel bars, where σ_s and f_y are the axial stress and yield stress, respectively. This factor is adopted to account for the adverse effects of bending moments and axial forces at the sliding plane of shear walls on the dowel action of vertical reinforcement. To avoid determining the rebar stress through complex iterative calculations, it is assumed that all boundary longitudinal rebars on the tensile side have reached the yielding state, i.e., the minimum strain ε_{wt} within the tensile boundary element is equal to the tensile yield strain ε_{yb} of the boundary longitudinal rebars, as shown in Fig. 8. The reasonableness of this assumption lies in the fact that if not all the tensile boundary longitudinal rebars

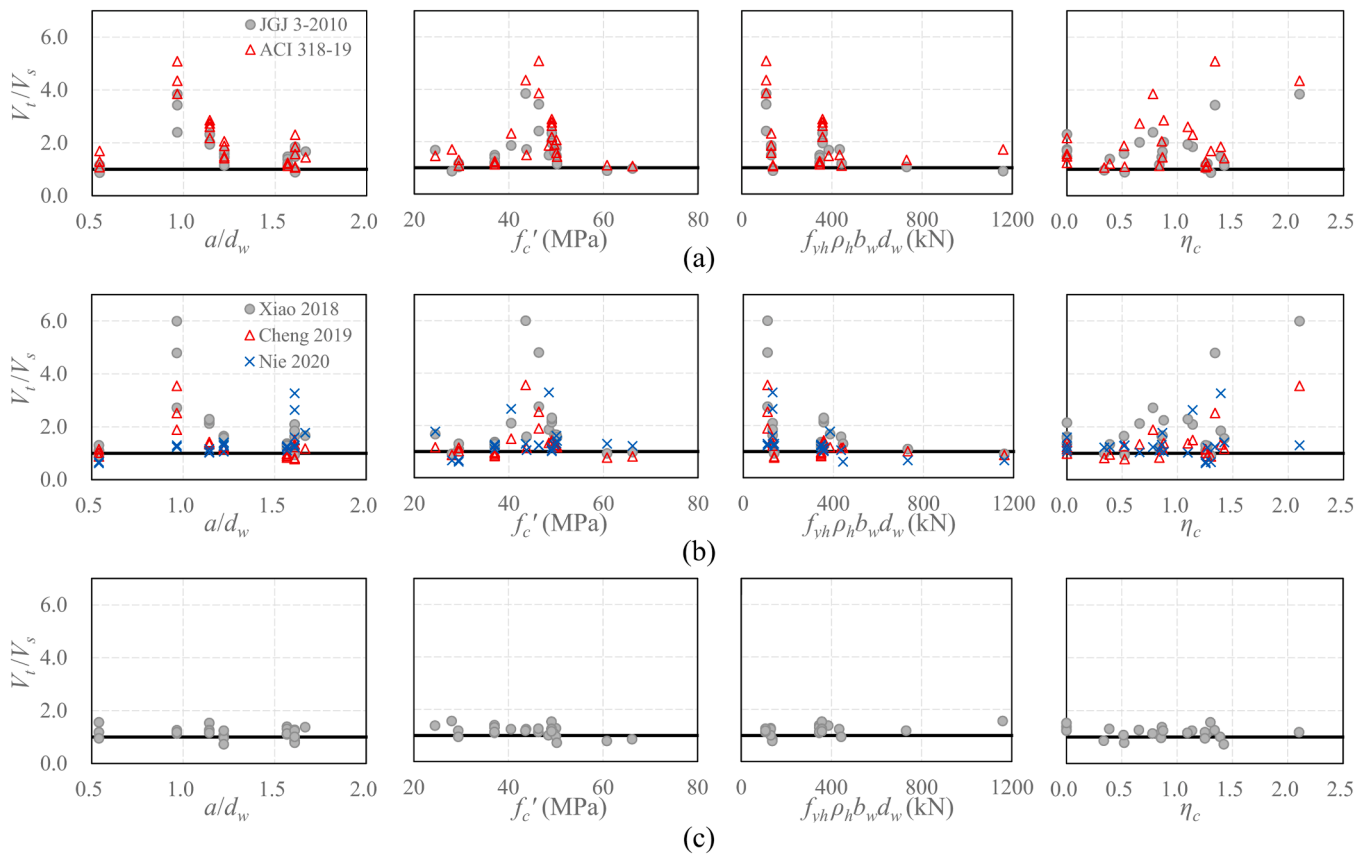

Fig. 9. Evaluation results of shear models for RC shear walls: (a) shear models of JGJ and ACI; (b) shear models by Xiao et al. [37], Cheng [38], and Nie et al. [2]; (c) proposed shear model.

Table 2
Statistical results for evaluation of shear models.

Model	Average	Maximum Value	Minimum Value	Standard deviation	Coefficient of variation
ACI 318 −19	2.03	5.09	1.06	1.09	0.53
JGJ 3 −2010	1.70	3.84	0.88	0.74	0.43
Xiao 2018	1.93	6.00	0.92	1.18	0.61
Cheng 2019	1.33	3.54	0.78	0.60	0.46
Nie 2020	1.32	3.27	0.62	0.57	0.44
Proposed	1.17	1.56	0.72	0.21	0.18

have yielded, the sliding capacity decreases with increasing strain in the tensile rebars. If the sliding failure occurs after all the tensile bars have yielded, the peak shear load-carrying capacity of the shear wall is determined by the ultimate flexural capacity, indicating the flexural-sliding failure mode. Therefore, the sliding capacity corresponding to the state shown in Fig. 8 provides a reasonable but conservative estimate of the sliding resistance of RC shear walls failed in sliding.

When the strain ε_{wt} and the compressive zone height c (obtained from Eq. (9)) are known, the maximum strain ε_{bc} and minimum strain ε_{wc} in the compressive boundary column can be determined based on the plane section assumption, as illustrated in Fig. 8. Consequently, the average stress in the compressive boundary longitudinal rebars $\sigma_{sb,c}$ (=Min $((\varepsilon_{bc}+\varepsilon_{wc})E_s/2, f_{yb})$), the average stress in the compressive vertical web rebars $\sigma_{sw,c}$ (=Min$(\varepsilon_{wc}E_s/2, f_{yw})$), and the average stress in the tensile vertical web rebars $\sigma_{sw,t}$ (=Min$(\varepsilon_{wt}E_s/2, f_{yw})$) can be calculated. On this basis, the shear wall sliding strength $V_{sl,p}$ can be predicted according to Eqs. (17) and (18), where the frictional resistance V_{fd} is computed using Eq. (15). It should be noted that, as the specimens in the collected database were not reinforced with inclined rebars, the proposed sliding model does not consider the contribution of inclined rebars to the sliding resistance.

$$V_{\mathrm{sl,p}} = \mathrm{V_{dd,p}} + \mathrm{V_{fd}} \tag{17}$$

$$\mathrm{V_{dd,p}} = \min\left\{\begin{array}{l} 1.3\left[A_{sb,c}\sqrt{f_c\left(1-\dfrac{\sigma_{sb,c}}{\mathrm{f_{yb}}}\right)\mathrm{f_{yb}}} + A_{sw,t}\sqrt{f_c\left(1-\dfrac{\sigma_{sw,t}}{2\mathrm{f_{yw}}}\right)\mathrm{f_{yw}}} + A_{sw,c}\sqrt{f_c\left(1-\dfrac{\sigma_{sw,c}}{2\mathrm{f_{yw}}}\right)\mathrm{f_{yw}}}\right], \\ 0.25\left[A_{sb,c}\left(1-\dfrac{\sigma_{sb,c}}{\mathrm{f_{yb}}}\right)f_{yb} + A_{sw,t}\left(1-\dfrac{\sigma_{sw,t}}{2\mathrm{f_{yw}}}\right)f_{yw} + A_{sw,c}\left(1-\dfrac{\sigma_{sw,c}}{2\mathrm{f_{yw}}}\right)f_{yw}\right] \end{array}\right\} \tag{18}$$

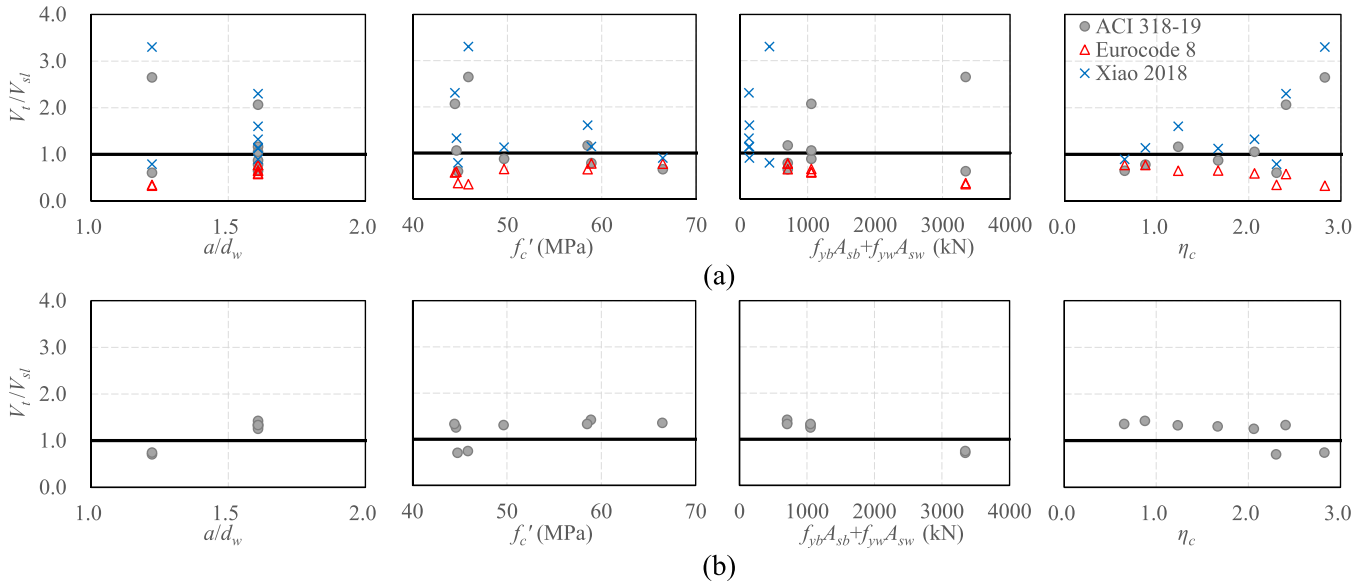

Fig. 10. Evaluation results of sliding models for shear walls: (a) existing sliding models; (b) proposed sliding model.

Table 3
Statistical results for evaluation of sliding models.

Model	Average	Maximum Value	Minimum Value	Standard deviation	Coefficient of variation
ACI 318 −19	1.23	2.65	0.61	0.74	0.60
Eurocode 8	0.59	0.77	0.33	0.17	0.29
Xiao 2018	1.56	3.30	0.79	0.85	0.54
Proposed	1.18	1.42	0.70	0.29	0.24

where $A_{sb,c}$ represents the area of compressive boundary longitudinal rebars, and $A_{sw,c}$, and $A_{sw,t}$ represent the areas of vertical web rebars under compression and tension, respectively. When calculating the reduction factor (1-σ_s/f_y), if the reinforcement stress σ_s is in tension, the corresponding yield stress f_y is taken as the tensile yield stress, and vice versa. The value of the reduction factor lies between 0 and 1.

4. Model evaluation and parametric analysis

4.1. Evaluation of shear models

Twenty-four shear wall specimens that experienced shear failure (including shear, shear-compression, and shear-sliding) were selected from the collected database for the evaluation of the existing and proposed shear models, with the results presented in Fig. 9 and Table 2. It should be noted that different models utilize different characteristic values for concrete strength. When evaluating these models based on experimental results, conversions between the compressive strength of different concrete specimens and between the concrete tensile and compressive strengths were determined using a simplified method proposed by Reineck et al. [55].

Fig. 9(a) and (b) present the evaluation results of the selected existing shear models (including the ACI, JGJ, Xiao, Cheng, and Nie shear models mentioned in Section 3.1). It can be observed that their ratios of the tested-to-predicted shear strength V_t/V_s decrease significantly with the increase of the shear contribution by horizontal distributed rebars $f_{yh}\rho_h b_w d_w$, which is adopted by each of the existing shear models. This indicates that the existing shear models cannot accurately reflect the influence of horizontal distributed rebars on the shear strength of shear walls under tension-shear. The ratios V_t/V_s of ACI, JGJ, Xiao, and Cheng shear models significantly increase with the increase of the concrete tensile ratio η_c, indicating that these models overestimate the adverse effect of axial tension on shear strength. The ratio V_t/V_s of the Nie shear model increases with the increase of the shear span-to-depth ratio a/d_w, indicating that it cannot accurately reflect the influence of a/d_w on shear strength. On the other hand, the coefficient of variation (COV) of V_t/V_s for the existing models ranges from 0.43 to 0.61, indicating a significant variability in their predictions compared to test results. The maximum values of V_t/V_s for the ACI and Xiao shear models are 5.09 and 6.00, respectively, while the minimum value for the Nie shear model is only 0.62, suggesting that excessive variability can lead to overly conservative or unsafe predictions.

As shown in Fig. 9(c), the V_t/V_s of the proposed shear model does not exhibit a significant upward or downward trend with variations in the shear span ratio a/d_w, concrete compressive strength f_c', and concrete tensile ratio η_c. This indicates that the proposed shear model can effectively capture the influence of shear span ratio, concrete strength, and axial tensile force on the shear strength of RC shear walls. Even though the proposed shear model does not directly adopt $f_{yh}\rho_h b_w d_w$ like the existing shear models, its V_t/V_s does not significantly change with an increase in $f_{yh}\rho_h b_w d_w$. This validates the rationale behind considering the enhancement of effective compressive strength of diagonal struts due to horizontal distributed reinforcement, indirectly accounting for the contribution of horizontal distributed reinforcement to the shear strength of shear walls. Moreover, the COV of V_t/V_s for the proposed shear model is only 0.18, significantly lower than those of the existing shear models, indicating its predictions demonstrate the highest accuracy.

4.2. Evaluation of sliding models

Using eight specimens that experienced sliding failure in the collected database, an evaluation was conducted on the selected existing sliding models. It should be noted that the JGJ sliding model predicted negative values for the sliding strength of several specimens, indicating an overestimation of the adverse effect of axial tension on sliding strength. This renders the predictions by the JGJ sliding model incomparable directly with other models. Thus, the evaluation results for the JGJ sliding model are not provided.

The evaluation results for the ACI, EC8, and Xiao sliding models are presented in Fig. 10 (a) and Table 3. It can be observed that the predictions by ACI and Xiao sliding models are relatively close. With an increase in concrete strength f_c' and concrete tensile ratio η_c, ratios of the

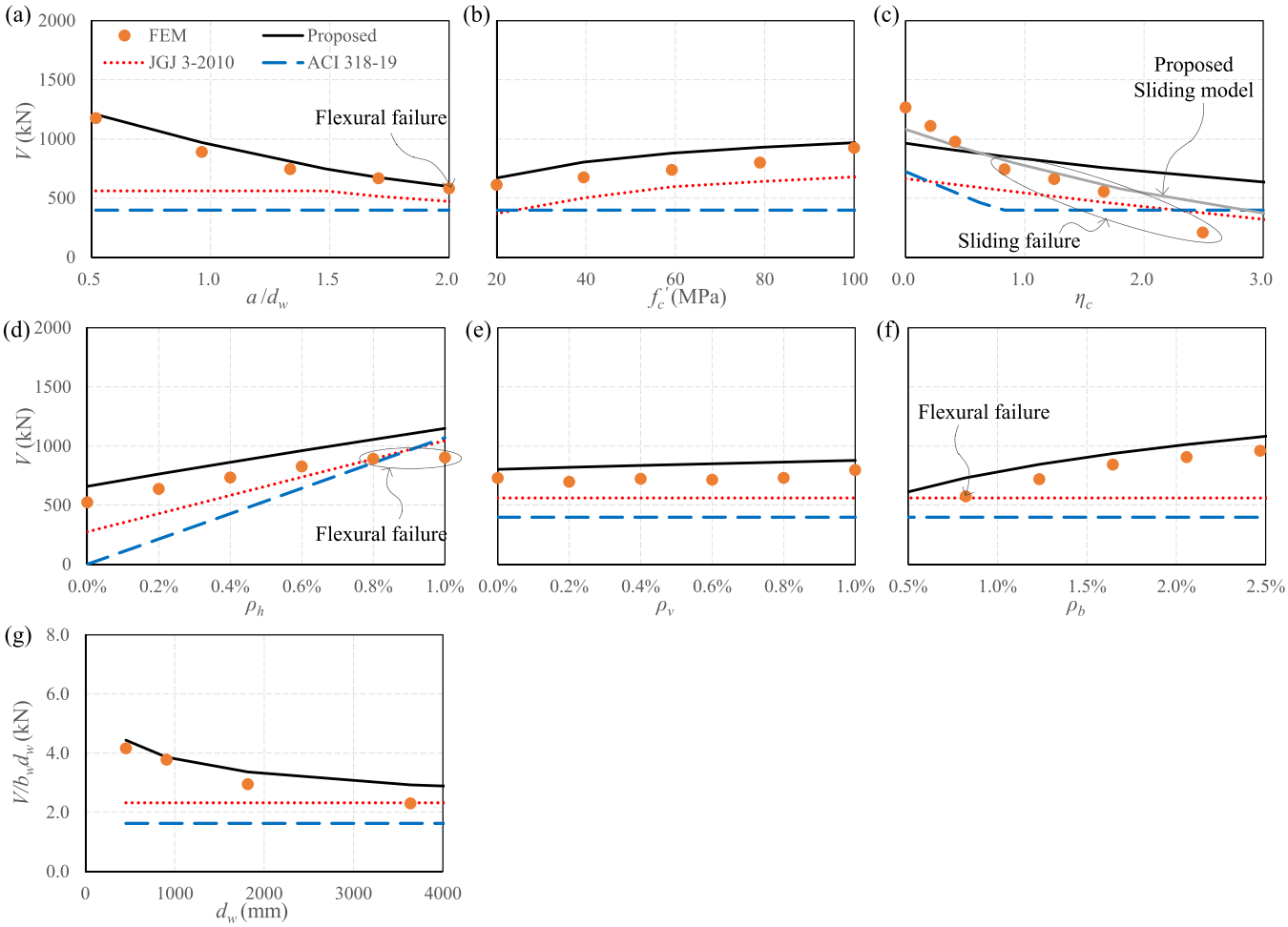

Fig. 11. Parameter Analysis of shear models: (a) shear span-to-depth ratio a/d_w, (b) cylinder concrete compressive strength f_c', (c) concrete tensile ratio η_c, (d) horizontal distributed reinforcement ratio ρ_h, (e) vertical distributed reinforcement ratio ρ_v, (f) boundary longitudinal reinforcement ratio ρ_b, (g) effective height d_w.

tested-to-predicted sliding strength V_t/V_{sl} show a certain trend of decrease and increase, respectively. This indicates that the ACI and Xiao sliding models cannot accurately reflect the influence of concrete strength and axial tension on the sliding capacity of shear walls. On the other hand, the EC8 sliding model significantly overestimates the sliding capacity of specimens, with a mean value of V_t/V_{sl} only reaching 0.59. Additionally, the EC8 sliding model fails to accurately reflect the contributions of the shear-span ratio and the yield capacity of vertical reinforcements ($f_{yb}A_{sb}+f_{yw}A_{sw}$) to the sliding capacity. The predictions of the ACI and Xiao sliding models are relatively more conservative than the EC8 sliding model, with mean values of V_t/V_{sl} being 1.23 and 1.56, respectively. However, both exhibit significant variability in their predictions, reflected in COVs exceeding 0.5. Overall, these three existing sliding models cannot effectively predict the sliding resistance of shear walls subjected to combined axial tension and lateral shear.

As shown in Fig. 10 (b), the ratios of tested-to-predicted sliding strength V_t/V_{sl} for the proposed sliding model do not exhibit significant changes with variations in a/d_w, f_c', $f_{yb}A_{sb}+f_{yw}A_{sw}$ and η_c. This indicates that the model can effectively reflect the influence of shear-span ratio, concrete strength, vertical reinforcements, and axial tension on the sliding strength of shear walls. From Table 3, it is evident that the proposed sliding model has a COV and mean value for V_t/V_{sl} of 0.24 and 1.18, respectively. The COV is significantly smaller than those of the existing sliding models, and the mean value is closest to 1. This suggests that the proposed sliding model demonstrates the highest predictive accuracy. The reason for this is that the proposed sliding model takes into account the interaction between the axial stress and dowel resistance of vertical rebars, correcting the overestimation of the rebar dowel contribution seen in the EC8 sliding model.

4.3. Parametric analysis of shear models

To further evaluate the proposed shear model, a parametric analysis was conducted, and the results were compared with numerical results and the predictions of the ACI and JGJ models, as shown in Fig. 11. The analysis was based on the parameter values of specimen SW2 tested by Ji et al. [1], with each analysis group changing only one parameter value. It should be noted that in the parametric analysis on the size effect, besides changing the effective height of the wall cross-section d_w, the wall height, reinforcement area, and axial tensile force were also proportionally adjusted to ensure consistent shear span-to-depth ratio a/d_w, reinforcement ratios (ρ_b, ρ_h, and ρ_v), and concrete tensile ratio η_c across different sizes of shear walls. The numerical models were subjected to horizontal monotonic loading, and shear failure occurred in all cases except for other failure modes indicated in the figure.

As shown in Fig. 11 (a), the lateral shear capacity of the numerical model decreased by 50.3 % as the shear span-to-depth ratio a/d_w increases from 0.5 to 2.0. The predictions of the proposed shear model closely match this decreasing trend, whereas the ACI and JGJ shear models significantly underestimate it. The reason for this is that the ACI model does not account for the effect of a/d_w, and the JGJ model only considers its impact when the ratio is greater than 1.5. In contrast, the

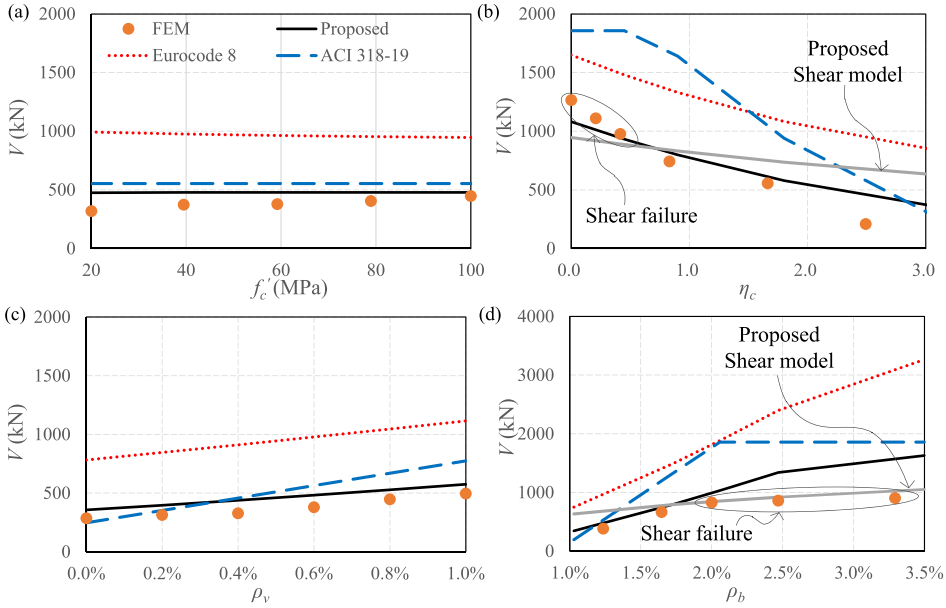

Fig. 12. Parameter Analysis of sliding models: (a) cylinder concrete compressive strength f_c', (c) concrete tensile ratio η_c, (e) vertical distributed reinforcement ratio ρ_v, (f) boundary longitudinal reinforcement ratio ρ_b.

proposed shear model accounts for the variation of the strut angle θ with a/d_w across its entire range. The numerical model indicates that when a/d_w exceeds 2.0, the failure mode of the shear wall transitions from shear failure to flexural failure. Therefore, predictions of the shear models for a/d_w greater than 2.0 are not evaluated.

Fig. 11 (b) shows the variation in shear capacity of the shear wall with changes in the cylinder concrete compressive strength f_c'. The numerical results indicate that when f_c' increased from 20 MPa to 100 MPa, the shear capacity increases by 50.9 %. The proposed and JGJ shear models predict increases in shear capacity of 44.8 % and 84.5 %, respectively, while the ACI shear model's prediction remains unchanged. Comparatively, the increase predicted by the proposed model is the closest to the numerical results. Due to the significant axial tensile force, the coefficient α_c in the ACI shear model decreases to zero, resulting in no influence of concrete strength on its shear capacity prediction. The JGJ shear model assumes that shear capacity is directly proportional to the axial concrete tensile strength f_t, but this still significantly overestimates the contribution of concrete strength to shear capacity compared to the numerical results. The proposed model not only considers the decrease in the strut effective coefficient β_s as the concrete strength increases, which determines the effective compressive strength $\beta_s f_c$' of the diagonal strut, but also takes into account the decrease in the strut width as the concrete strength increases (under the premise of constant vertical reinforcement area).

Fig. 11 (c) shows that the shear capacity of the numerical model significantly decreases with the increase in the concrete tensile ratio η_c (representing the axial tensile force), and the failure mode transitions from shear failure to sliding failure. Therefore, the figure includes the predicted results of both the proposed shear and sliding models, with their intersection occurring at approximately η_c= 0.62. When η_c> 0.62, the predicted capacity of the proposed sliding model is lower than that of the shear model, indicating that the shear wall undergoes sliding failure. Conversely, when η_c< 0.62, the predicted capacity of the proposed shear model is lower than that of the sliding model, indicating the shear failure. The failure mode predicted by the proposed models aligns with the numerical results, as shown in Fig. 11 (c). It is important to note that when η_c is between 0.4 and 1.0, the difference in capacity predictions between the proposed shear and sliding models is not substantial, making it challenging to accurately determine the failure mode solely based on the relative predicted capacities. The failure mode may also vary due to the randomness of material mechanical properties, crack development, and loading history.

As shown in Fig. 11 (d), the shear capacity of the proposed, JGJ, and ACI shear models all increase with the horizontal distributed reinforcement ratio ρ_h. The ACI model shows the largest increase in shear capacity, followed by the JGJ model, while the proposed model shows the smallest increase but is the closest to the numerical predictions. Specifically, when ρ_h is small (less than 0.4 %), both the ACI and JGJ models significantly underestimate the shear capacity predicted by the numerical model. When ρ_h is greater than 0.8 %, the shear capacity of the numerical model no longer increases because the failure mode of the shear wall has transitioned to flexural failure. On the other hand, the influence of the vertical distributed reinforcement ratio ρ_v on the shear capacity of shear walls is relatively minor, as shown in Fig. 11 (e). When ρ_v increased from 0 to 1.0 %, the shear capacity of the numerical model increases by 9.4 %, while the proposed model shows an increase of 7.0 %. However, the ACI and JGJ models completely ignored the effect of ρ_v. It is worth noting that the comparison also indicates that ignoring the influence of ρ_v on the shear capacity of RC shear walls under tension-shear is reasonable for simplification.

The numerical results in Fig. 11 (f) indicate that an increase in the boundary longitudinal reinforcement ratio ρ_b can significantly enhance the shear capacity of shear walls. The proposed shear model, which considers the effect of boundary longitudinal reinforcement on the diagonal strut width, accurately reflects the influence of ρ_b on shear capacity. In contrast, the ACI and JGJ models do not account for the impact of boundary longitudinal reinforcement.

Fig. 11 (g) shows the effect of size on the shear strength of the shear walls under tension-shear. The numerical model indicates that as the effective height d_w increases (from 455 mm to 3636 mm), its nominal shear stress decreases by 47.4 %. The proposed shear model accounts for the size effect through the effective strut coefficient β_s, although it slightly underestimates the reduction in shear strength compared to the numerical model. The ACI and JGJ models do not consider the size effect.

4.4. Parametric analysis of sliding models

The parametric analysis of the sliding model was conducted based on the parameter values of the specimen SW4 tested by Ji et al. [1], with

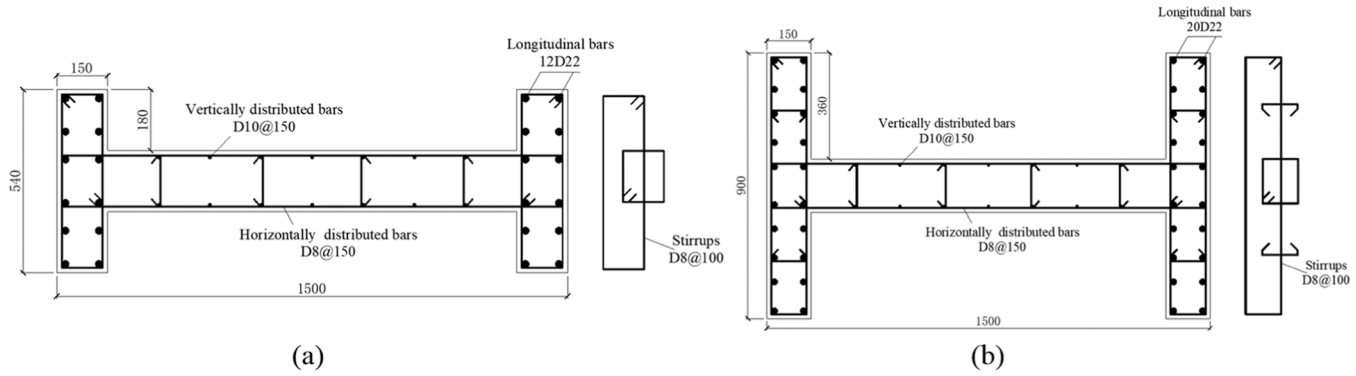

Fig. 13. Cross-sections of shear walls with flanges: (a) SW2–3 W; (b) SW2–5 W.

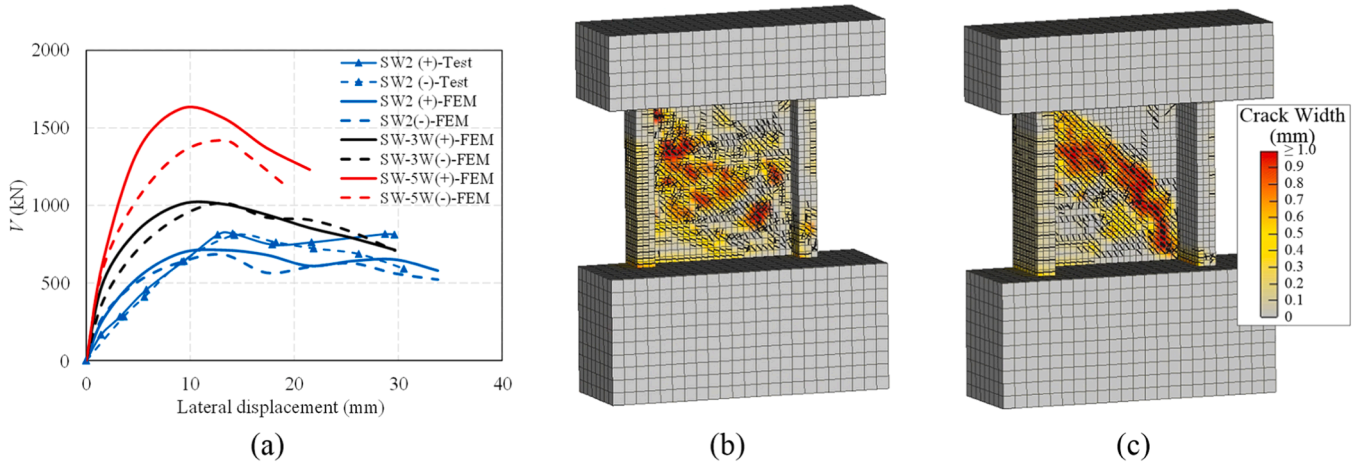

Fig. 14. Numerical results of shear walls with flanges: (a) skeleton curves of shear load *V* versus lateral displacement; crack distribution and width for (b) SW2–3 W and (c) SW2–5 W at peak shear loads.

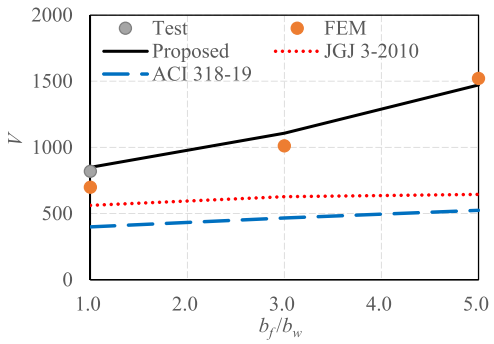

Fig. 15. Influence of flange width on tension-shear strength of shear walls.

each analysis group changing only one parameter value. The predicted results of the proposed, ACI and EC8 sliding models are shown in Fig. 12, as well as the numerical results. Since the sliding failure surface is a horizontal cross-section, the effects of the shear span-to-depth ratio and horizontal distributed reinforcement on sliding capacity can be ignored. Additionally, neither the existing nor the proposed sliding models consider the size effect, so sensitivity analysis for these three parameters was not conducted. The numerical models were subjected to monotonic loading, and sliding failure occurred in all cases except where other failure modes noted in the figure.

Fig. 12 (a) shows the effect of cylinder concrete compressive strength f_c' on sliding capacity. As f_c' increases, the sliding capacity of the numerical model exhibits a certain degree of increase. In contrast, the sliding capacities of the proposed and ACI sliding models remain almost unchanged with varying concrete strength, with the proposed model's predictions being the closest to the numerical results. Conversely, the sliding capacity predicted by the EC8 sliding model shows a decreasing trend and significantly overestimates the numerical results.

Fig. 12 (b) compares the changes in sliding capacity with the increase in concrete tensile ratio η_c. It can be seen that the proposed sliding model aligns best with the numerical results. The transition of failure modes with η_c has been discussed in detail in Section 4.3, so it will not be elaborated here.

As shown in Fig. 12 (c), as the vertical distributed reinforcement ratio ρ_v increases from zero to 1.0 %, the sliding capacity of the numerical model increases by 73.5 %. The sliding capacities of the proposed, ACI, and EC8 models increase by 61.3 %, 213.5 %, and 42.5 %, respectively. Therefore, the proposed model better reflects the influence of ρ_v on the sliding capacity of RC shear walls under tension-shear.

Fig. 12 (d) shows that as the boundary longitudinal reinforcement ratio ρ_b increases, the lateral capacity of the shear wall significantly improves in the numerical model, accompanied by a transition in failure mode from sliding failure to shear failure. The figure provides the predicted lateral capacities of the proposed sliding and shear models, which are equal at approximately ρ_b= 1.7 %. When ρ_b< 1.7 %, the predicted lateral capacity of the proposed sliding model is lower than that of the proposed shear model, indicating that the shear wall is controlled by sliding failure. Conversely, when ρ_b> 1.7 %, the shear wall is controlled by shear failure. This is consistent with the transition in failure modes shown by the numerical model with increasing ρ_b.

5. Effect of boundary flanges on shear strength

In the existing tension-shear tests for RC shear walls, only specimens with a rectangular section have been tested. However, RC shear walls are typically reinforced with boundary flanges, which can significantly enhance the shear strength. To investigate the influence of boundary flanges on the tension-shear capacity of shear walls, this study conducted a numerical analysis using nonlinear FE methods on H-shaped shear walls with flanges. Considering that the flange may increase the difference between cyclic and monotonic responses of RC shear walls, the FE models for non-rectangular shear walls were subjected to cyclic loading.

Based on the rectangular shear wall specimen SW2 tested by Ji et al. [1], two H-shaped shear wall specimens with different flange widths were designed, as illustrated in Fig. 13. The longitudinal reinforcement ratio of their boundary flanges was kept consistent with that of the boundary columns in specimen SW2. The material and geometric parameters, as well as the target axial force, were also maintained in accordance with those of WS2. Using the validated FE methods described in Section 2.2, numerical simulations were conducted for the H-shaped shear walls, and the results are presented in Fig. 14. It can be observed that both specimens experience shear failure, and increasing the flange width significantly enhances the shear capacity and stiffness.

Fig. 15 presents the experimental and numerical shear strength for SW2, SW2–3 W, and SW2–5 W, along with the predictions from the JGJ, ACI, and the proposed shear models. It can be observed that the upward trend in shear strength predicted by the proposed model closely aligns with the FE results. In contrast, the predictions of the JGJ and ACI shear models significantly underestimate the contribution of the flange to the shear strength of the shear walls. This is attributed to the fact that the proposed shear model directly considers the contribution of the compressed flange to the diagonal strut capacity. However, the JGJ and ACI shear models only account for the reduction in nominal axial tensile stress caused by the flange without directly considering its contribution to the shear strength of shear walls.

According to existing research [56–58], the shear lag effect has a significant impact on the flexural strength and stiffness of flanged RC shear walls. The proposed shear model is effectively validated by the numerical results within the range where the ratio of flange width to web thickness b_f/b_w is less than 5, under the condition that the FE model can inherently consider the shear lag effect. This indicates that it is feasible for the proposed shear model to ignore the shear lag effect within the range of $b_f/b_w \leq 5.0$. However, for larger flange widths, the shear lag effect may have a significant impact on the shear strength of flanged RC shear walls, which requires further research.

6. Summary and conclusions

(1) This paper established a test database comprising 41 RC shear walls subjected to combined axial tension and lateral shear. The collected tests were categorized based on failure modes, serving as the foundation for evaluating shear and sliding models for RC shear walls.

(2) Based on the mechanics-based cracking strut-and-tie model, a simplified shear model applicable to RC shear walls under tension-shear was proposed. This model considers the influence of horizontal reinforcement, concrete strength, and size effects on shear strength through the effective strut coefficient. It also incorporates the effects of axial tensile load and vertical reinforcement through the strut width and accounts for the influence of flange width through the equivalent strut thickness.

(3) Evaluation of the shear models based on the collected database revealed that the selected existing shear models exhibited significant variability in predicting the shear strength, with coefficients of variation between 0.43 and 0.61 for the ratios of the tested-to-predicted shear strength. In contrast, the proposed shear model demonstrated a much lower coefficient of variation of 0.18.

(4) Evaluation of the sliding models based on the collected database indicated that the existing sliding models were not effective in predicting the sliding resistance of shear walls under tension-shear. A modified sliding model was proposed based on the sliding model in Eurocode 8, considering the weakening effect of axial stress on the dowel resistance of vertical reinforcement. The proposed sliding model was validated to better predict the sliding strength of RC shear walls.

(5) A parametric analysis was conducted on the proposed models and the code models, and finite element results were used for verification. The results indicated that the proposed models not only effectively captured the influence of shear span-to-depth ratio, concrete strength, reinforcement ratios, and axial tensile force on the shear and sliding capacities of RC shear walls, but also well reflected the transition of shear and sliding failure modes.

(6) Numerical analysis demonstrated that increasing the flange width significantly enhances the shear strength and stiffness of shear walls. The proposed shear model was validated to effectively capture the increased shear capacity due to the widening of the flange width in shear walls under tension-shear. However, the shear models provided by ACI 318-19 and JGJ 3-2010 notably underestimated this effect.

CRediT authorship contribution statement

Wei-Jian Yi: Writing – review & editing, Supervision, Conceptualization. **Zhongguo John Ma:** Writing – review & editing, Supervision. **Yun Zhou:** Writing – review & editing. **Hui Chen:** Writing – review & editing, Visualization, Validation, Software, Methodology, Funding acquisition, Conceptualization. **Jing-Ming Sun:** Writing – review & editing, Software, Investigation, Formal analysis. **Ya-Bo Ding:** Writing – original draft, Methodology, Investigation, Formal analysis, Data curation.

Declaration of Competing Interest

The authors declared that they have no conflicts of interest to this work.

Data availability

Data will be made available on request.

Acknowledgement

The authors would like to acknowledge the financial support provided for this work by the National Natural Science Foundation of China (Nos. 52008161), China Postdoctoral Science Foundation (Nos. 2021T140196), and Education Department of Hunan Province of China (No. 21C0367).

References

[1] Ji X, Cheng X, Xu M. Coupled axial tension-shear behavior of reinforced concrete walls. Eng Struct 2018;167:132–42.
[2] Nie X, Wang J-J, Tao M-X, Fan J-S, Mo Y, Zhang Z-Y. Experimental study of shear-critical reinforced-concrete shear walls under tension-bending shear-combined cyclic load. J Struct Eng 2020;146:04020047.
[3] Rojas F, Naeim F, Lew M, Carpenter LD, Youssef NF, Saragoni GR, et al. Performance of tall buildings in Concepción during the 27 February 2010 moment magnitude 8.8 offshore Maule, Chile earthquake. Struct Des Tall Spec Build 2011; 20:37–64.
[4] Song C, Pujol S, Lepage A. The collapse of the Alto Río building during the 27 February 2010 Maule, Chile, earthquake. Earthq Spectra 2012;28:301–34.
[5] Deger ZT, Wallace JW. Collapse assessment of the Alto Rio building in the 2010 Chile earthquake. Earthq Spectra 2015;31:1397–425.

[6] Zhang P, Restrepo JI, Conte JP, Ou J. Nonlinear finite element modeling and response analysis of the collapsed Alto Rio building in the 2010 Chile Maule earthquake. Struct Des Tall Spec Build 2017;26:e1364.
[7] Mo Y, Chan J. Behavior of reinforced-concrete-framed shear walls. Nucl Eng Des 1996;166:55–68.
[8] Barda F. Shear strength of low-rise walls with boundary elements. Lehigh University,; 1972.
[9] Orakcal K, Massone LM, Wallace JW. Shear strength of lightly reinforced wall piers and spandrels. Acids Struct J 2009;106:455.
[10] Luna B., Whittaker A., Rivera J. Seismic behavior of low aspect ratio reinforced concrete shear walls. 2013.
[11] Looi D, Su R, Cheng B, Tsang H. Effects of axial load on seismic performance of reinforced concrete walls with short shear span. Eng Struct 2017;151:312–26.
[12] Luna BN, Whittaker AS. Peak strength of shear-critical reinforced concrete walls. Acids Struct J 2019.
[13] Kim J-H, Park H-G. Shear and shear-friction strengths of squat walls with flanges. Acids Struct J 2020;117:269–80.
[14] Cheng M-Y, Wibowo LS, Giduquio MB, Lequesne RD. Strength and deformation of reinforced concrete squat walls with high-strength materials. American Concrete Institute,; 2021.
[15] Kim J-H, Park H-G. Shear strength of flanged squat walls with 690 MPa reinforcing bars. Acids Struct J 2022;119:209–20.
[16] Faraone G, Hutchinson TC, Piccinin R, Silva JF. Seismic performance of varying aspect ratio full-scale concrete walls. Acids Struct J 2022;119.
[17] Oesterle RG, Fiorato AE, Johal LS, et al. Earthquake resistant structural walls-tests of isolated walls[J]. Research and Development Construction Technology Laboratories, Portland Cement Association,; 1976.
[18] Oesterle RG, Aristizabal-Ochoa JD, Fiorato AE, et al. Earthquake resistant structural walls-tests of isolated walls-phase II[J]. Construction Technology Laboratories, Portland Cement Association,; 1979.
[19] Gulec C.K., Whittaker A.S. Performance-based assessment and design of squat reinforced concrete shear walls: MCEER; 2009.
[20] Del Carpio Ramos M, Whittaker AS, Gulec CK. Predictive equations for the peak shear strength of low-aspect ratio reinforced concrete walls. J Earthq Eng 2012;16:159–87.
[21] Grammatikou S, Biskinis D, Fardis MN. Strength, deformation capacity and failure modes of RC walls under cyclic loading. Bull Earthq Eng 2015;13:3277–300.
[22] Ning CL, Li B. Probabilistic development of shear strength model for reinforced concrete squat walls. Earthq Eng Struct Dyn 2017;46:877–97.
[23] Moretti ML, Kono S, Obara T. On the Shear Strength of Reinforced Concrete Walls. ACI Structural Journal. 2020;117.
[24] Deger ZT, Basdogan C. Empirical equations for shear strength of conventional reinforced concrete shear walls. Acids Struct J 2021;118:61–71.
[25] Chetchotisak P, Chomchaipol W, Teerawong J, Shaingchin S. Strut-and-tie model for predicting shear strength of squat shear walls under earthquake loads. Eng Struct 2022;256:114042.
[26] Abdullah S.A., Wallace J.W. UCLA-Rcwalls database for reinforced concrete structural walls[C]//Proceedings of the 11th national conference in earthquake engineering. 2018.
[27] Wang T, Lai T, Zhao H, Lin H, Wang Y. Tensile-shear mechanical performance test of reinforced concrete shear wall. Build Struct 2017;47(2):64–9.
[28] Ren C, Xiao C, Xu P. Experimental study on tension-shear performance of reinforced concrete shear wall. China Civ Eng J 2018;51(4):20–33.
[29] Xie Yuejun. Experimental study on seismic behaviour of low-rise reinforced concrete shear walls. Guangzhou: South China University of Technology,; 2018 (B. S. Dissertation [in Chinese]).
[30] Cheng X, Ji X, Henry RS, Xu M. Coupled axial tension-flexure behavior of slender reinforced concrete walls. Eng Struct 2019;188:261–76.
[31] Ji X, Xu M, Cheng X, Miao Z. Experimental study on axial tension-flexure-shearbehavior of moderate-aspect-ratio RC shear walls. J Build Struct 2021;42:90–101 ([in Chinese]).
[32] Yao Z, Fang X, Wei H. Experimental study on shear behavior of reinforced concrete shear walls under eccentric tension. J Build Struct 2020;41(4):71–81.
[33] Wei F, Chen H, Xie Y. Experimental study on seismic behavior of reinforced concrete shear walls with low shear span ratio. J Build Eng 2022;45:103602.
[34] Ke XJ, Huang Z, Wang QB, Meng CL. Performance and strength analysis of shear walls with vertical steel encased profiles under tensile-shear load. J Build Eng 2023;79:107823.
[35] ACI Committee 318. Building code requirements for structural concrete (ACI 318-19): Commentary on building code requirements for structural concrete (ACI 318R-19). Farmington Hills, MI: American Concrete Institute,; 2019. p. 623.
[36] JGJ3-2010. Technical specification for concrete structures of tall building. China Architecture & Building Press Beijing,; 2010.
[37] Xiao C, Xu P, Ren C. Analysis of tension-shear capacity of reinforced concrete shear wall. China Civ Eng J 2018;51:26–36.
[38] Cheng Xiaowei. Study on tension-shear and tension-flexure behavior of reinforced concrete walls. Beijing: Tsinghua University,; 2019 (Ph.D.Dissertation [in Chinese]).
[39] Červenka J, Papanikolaou VK. Three dimensional combined fracture–plastic material model for concrete. Int J Plast 2008;24:2192–220.
[40] Bazant ZP, Oh BH. Crack band theory for fracture of concrete. Matér Et Constr 1983;16:155–77.
[41] Chen H, Yi W-J, Ma ZJ. Shear size effect in simply supported RC deep beams. Eng Struct 2019;182:268–78.
[42] Menetrey P, Willam KJ. Triaxial failure criterion for concrete and its generalization. Acids Struct J 1995;92:311–8.
[43] Jendele L, Cervenka J. Finite element modelling of reinforcement with bond. Comput Struct 2006;84:1780–91.
[44] Vecchio FJ, Collins MP. The modified compression-field theory for reinforced concrete elements subjected to shear. Acids J 1986;83:219–31.
[45] Bentz EC, Vecchio FJ, Collins MR. Simplified modified compression field theory for calculating shear strength of reinforced concrete elements. Acids Struct J 2006;103:614–24.
[46] Cervenka V, Jendele L, Cervenka J. ATENA Program Documentation, Part 1: Theory, 2013. Prague: Cervenka Consulting Ltd,; 2012.
[47] Nguyen PT. A study of shear behavior of reinforced concrete deep beams. Austin, the US: The University of Texas at Austin,; 2013.
[48] Cervenka V, Cervenka J, Jendele L, Smilauer V. ATENA simulation of crack propagation in CONCRACK benchmark. European. J Environ Civ Eng 2014;18:828–44.
[49] Yi W-J, Huang B, Chen H. Finite element analysis on the effect of web reinforcement on shear failure of reinforced concrete continuous deep beams. Chin J Comput Mech 2017;34:175–82.
[50] Chen H, Yi W-J, Ma ZJ, Hwang H-J. Modeling of shear mechanisms and strength of concrete deep beams reinforced with FRP bars. Compos Struct 2020;234:111715.
[51] Yi W-J, Li Y, Chen H, Ma ZJ, Zhou K-J, Huang Y, et al. Shear strength evaluation of RC D-Regions based on Single-Panel Strut-and-Tie model. Eng Struct 2022;265:114500.
[52] Chen H, Yi W-J, Hwang H-J. Cracking strut-and-tie model for shear strength evaluation of reinforced concrete deep beams. Eng Struct 2018;163:396–408.
[53] Chen H, Yi W-J, Ma ZJ. Shear-transfer mechanisms and strength modeling of RC continuous deep beams. J Struct Eng 2020;146:04020240.
[54] Standard B. Eurocode 8: Design of structures for earthquake resistance. Part 2005:1998–2001.
[55] Reineck KH, Kuchma DA, Kim KS, Marx S. Shear database for reinforced concrete members without shear reinforcement. Acids Struct J 2003;100:240–9.
[56] Khaloo A, Tabiee M, Abdoos H. A numerical laboratory for simulation of flanged reinforced concrete shear walls. Numer Methods Civ Eng 2021;6:92–102.
[57] Ma J, Ning C-L, Li B. Peak shear strength of flanged reinforced concrete squat walls. J Struct Eng 2020;146:04020037.
[58] Kwan AK. Shear lag in shear/core walls. J Struct Eng 1996;122:1097–104.